Physical Links from Atmospheric Circulation Patterns to Barents–Kara Sea Ice Variability from Synoptic to Seasonal Timescales in the Cold Season

PETER YU FENG SIEW,[a] YUTIAN WU,[a] MINGFANG TING,[a] CHENG ZHENG,[a] ROBIN CLANCY,[b] NATHAN T. KURTZ,[c] AND RICHARD SEAGER[a]

[a] *Lamont-Doherty Earth Observatory, Columbia University, Palisades, New York*
[b] *University of Washington, Seattle, Washington*
[c] *Cryospheric Sciences Laboratory, NASA Goddard Space Flight Center, Greenbelt, Maryland*

(Manuscript received 16 March 2023, in final form 4 July 2023, accepted 24 August 2023)

ABSTRACT: Previous findings show that large-scale atmospheric circulation plays an important role in driving Arctic sea ice variability from synoptic to seasonal time scales. While some circulation patterns responsible for Barents–Kara sea ice changes have been identified in previous works, the most important patterns and the role of their persistence remain unclear. Our study uses self-organizing maps to identify nine high-latitude circulation patterns responsible for day-to-day Barents–Kara sea ice changes. Circulation patterns with a high pressure center over the Urals (Scandinavia) and a low pressure center over Iceland (Greenland) are found to be the most important for Barents–Kara sea ice loss. Their opposite-phase counterparts are found to be the most important for sea ice growth. The persistence of these circulation patterns helps explain sea ice variability from synoptic to seasonal time scales. We further use sea ice models forced by observed atmospheric fields (including the surface circulation and temperature) to reproduce observed sea ice variability and diagnose the role of atmosphere-driven thermodynamic and dynamic processes. Results show that thermodynamic and dynamic processes similarly contribute to Barents–Kara sea ice concentration changes on synoptic time scales via circulation. On seasonal time scales, thermodynamic processes seem to play a stronger role than dynamic processes. Overall, our study highlights the importance of large-scale atmospheric circulation, its persistence, and varying physical processes in shaping sea ice variability across multiple time scales, which has implications for seasonal sea ice prediction.

SIGNIFICANCE STATEMENT: Understanding what processes lead to Arctic sea ice changes is important due to their significant impacts on the ecosystem, weather, and shipping, and hence our society. A well-known process that causes sea ice changes is atmospheric circulation variability. We further pin down what circulation patterns and underlying mechanisms matter. We identify multiple circulation patterns responsible for sea ice loss and growth to different extents. We find that the circulation can cause sea ice loss by mechanically pushing sea ice northward and bringing warm and moist air to melt sea ice. The two processes are similarly important. Our study advances understanding of the Arctic sea ice variability with important implications for Arctic sea ice prediction.

KEYWORDS: Arctic; Sea ice; Atmospheric circulation; Ice loss/growth; Ice thickness

1. Introduction

Sea ice reflects a large portion of incoming solar radiation and acts as an insulating layer that reduces the exchange of mass, heat, and moisture between the atmosphere and ocean, and hence plays a crucial role in regulating the climate system. Arctic sea ice loss over recent decades (Notz et al. 2020) has been shown to impact Arctic ecosystems (Post et al. 2013), coastal erosion (Kostopoulos et al. 2018), increased Arctic precipitation (Bintanja and Selten 2014; Kopec et al. 2016), and Arctic surface warming (Kim and Kim 2017; Screen and Simmonds 2010), and potentially influences midlatitude circulation (Cohen et al. 2014; Siew et al. 2020; Outten et al. 2023). Such important climate impacts prompt us to understand what processes are responsible for Arctic sea ice loss over the past decades and variability across various time scales.

Over synoptic to seasonal time scales, sea ice changes are largely shaped by large-scale atmospheric circulation via thermodynamic and dynamic pathways (e.g., Fang and Wallace 1994; Sorteberg and Kvingedal 2006; Serreze and Stroeve 2015; Park et al. 2018), but their relative contributions are not entirely clear. The thermodynamic pathway refers to atmospheric heat and moisture transports that perturb surface energy fluxes and thus contribute to sea ice melt or freeze. The role of enhanced moisture transport and downward longwave radiation in driving Arctic sea ice loss has been highlighted in recent studies (e.g., Woods et al. 2013; Mortin et al. 2016; Woods and Caballero 2016; Park et al. 2015; Hegyi and Taylor 2018; Yang and Magnusdottir 2017; Liu et al. 2022; Zheng et al. 2022). The dynamic pathway refers to wind-driven sea ice motions and redistribution, whose importance is also well recognized (e.g., Jung and Hilmer 2001; Rigor et al. 2002; Park et al. 2015; Park and Stewart 2016; Cai et al. 2020; Jiang et al. 2021). The two pathways contributing to sea ice changes

Supplemental information related to this paper is available at the Journals Online website: https://doi.org/10.1175/JCLI-D-23-0155.s1.

Corresponding author: Peter Yu Feng Siew, pyfsiew@ldeo.columbia.edu

DOI: 10.1175/JCLI-D-23-0155.1

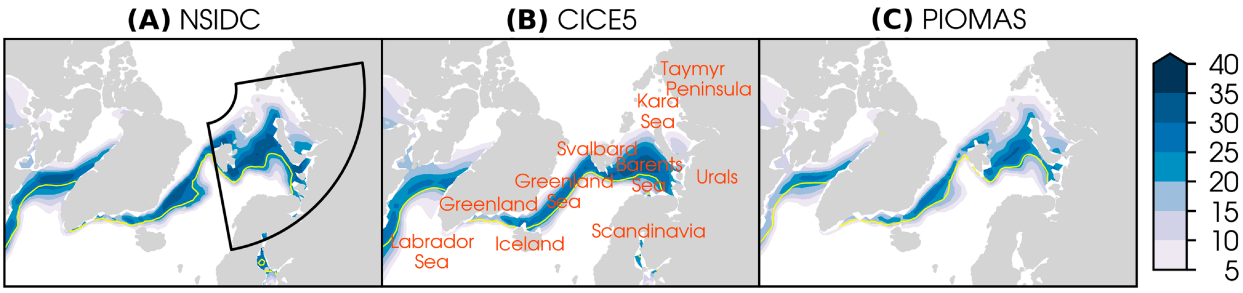

FIG. 1. Sea ice concentration climatology and daily variability. Climatological sea ice extent (yellow lines show 15% concentration) and standard deviation of daily sea ice concentration (shading) in DJFM from (a) NSIDC satellite observations and sea ice models (b) CICE5 and (c) PIOMAS. The black box in (a) shows the Barents–Kara Sea region (65°–85°N, 10°–100°E) for computing the area-averaged sea ice index.

are closely related (Holland and Kwok 2012; Holland and Kimura 2016; Polyakov et al. 2022). While isolating the two pathways using observations remains difficult, sea ice models have been found to be a useful tool. For example, sea ice models forced by observed atmospheric conditions can largely reproduce the observed sea ice variability, thus allowing us to diagnose the two different pathways and relevant processes (Ding et al. 2017; Lee et al. 2019; Clancy et al. 2022; Lim et al. 2022a; Liang et al. 2022).

The large-scale atmospheric circulation exhibits various circulation patterns that could modulate the physical pathways shaping Arctic sea ice variability (Mills and Walsh 2014; Yu et al. 2019). Previous studies have identified some circulation patterns that are important for Barents–Kara sea ice loss. A typical one is a low pressure system over Greenland and a high pressure system over Scandinavia (Woods et al. 2013; Luo et al. 2017; Wang et al. 2020; Zheng et al. 2022). Other sea ice loss patterns have also been identified, including the positive phase of the North Atlantic Oscillation (Deser et al. 2000; Rigor et al. 2002; Park et al. 2018), Ural-Scandinavian blocking episodes (Luo et al. 2016; Gong and Luo 2017; Tyrlis et al. 2019; Chen et al. 2018), and Arctic cyclones moving along the west of the sea ice basins (Sorteberg and Walsh 2008; Boisvert et al. 2016; Rinke et al. 2017; Madonna et al. 2020; Schreiber and Serreze 2020; Finocchio et al. 2022; Clancy et al. 2022). Nevertheless, a systematic approach identifying the most responsible circulation patterns and their physical processes shaping Barents–Kara sea ice loss and growth across multiple time scales is still missing.

In the present study, we use a clustering approach, self-organizing maps (SOM), to identify various circulation patterns in the Euro-Atlantic sector that are important for day-to-day Barents–Kara sea ice changes (both ice loss and growth). We extend these daily linkages to seasonal time scales by accounting for the persistence of these circulation patterns. We also use sea ice models to assess the relative contributions of thermodynamic and dynamic processes responsible for the circulation–ice linkages. We focus on the ice growth season (December–March) and the Barents and Kara Seas where sea ice experiences the largest variability (Fig. 1).

We begin with a description of data and methods (section 2), including the SOM approach and sea ice models. We next reveal the high-latitude circulation patterns and their effects on Barents–Kara sea ice changes on weather time scales (section 3a) and the underlying mechanisms (section 3b). How the persistence of circulation patterns modulates sea ice changes on seasonal time scales is presented in section 3c. We end with discussion and concluding remarks in section 4.

2. Data and methods

a. *Observations and sea ice models*

We use the National Aeronautics and Space Administration (NASA) Modern-Era Retrospective Analysis for Research and Applications version 2 (MERRA-2; Gelaro et al. 2017) for daily atmospheric variables through the winter season [December–March (DJFM)] from 1980/81 to 2020/21. We find similar results when using another reanalysis dataset, the European Centre for Medium-Range Weather Forecasts (ECMWF) reanalysis ERA5 (Hersbach et al. 2020), and hence only results from MERRA-2 will be shown. We use the National Oceanic and Atmospheric Administration (NOAA) National Snow and Ice Data Center (NSIDC) Climate Data Record of Passive Microwave Sea Ice Concentration version 4 (Meier et al. 2021) for the daily sea ice concentration (SIC) in the same period. The satellite data were available every two days before July 1987 and hence temporal interpolation was applied to obtain daily resolution (Meier et al. 2022). The satellite sea ice product has 54 days (including most days in 1987/88 December and January) missing during the period of interest.

We also use two sea ice models: CICE5 (covering the period 1980/81–2017/18; Bailey et al. 2018) and PIOMAS version 2.1 (covering the period 1980/81–2020/21; Zhang and Rothrock 2003) to obtain simulated sea ice concentration and other variables such as sea ice thickness and ice drifts whose daily and spatial coverages are incomplete from observations. CICE5 (PIOMAS) has a mean horizontal resolution of 1° (22 km) in the Arctic. CICE5 coupled with a slab-ocean model (i.e., without ocean circulation) is forced by atmospheric surface fields such as surface winds, temperature, and energy fluxes from the Japanese 55-year Reanalysis (JRA-55; Kobayashi et al. 2015). PIOMAS coupled with a dynamic ocean model is forced by similar atmospheric surface fields from the National Centers for Environmental Prediction–National Center for Atmospheric Research

(NCEP–NCAR) reanalysis (Kalnay et al. 1996) and further assimilates satellite sea ice concentration (Zhang and Rothrock 2003). The simulated sea ice concentration can largely reproduce the observed sea ice climatology and variability (Fig. 1) by responding to the realistic atmospheric forcing. Nevertheless, the sea ice edge (yellow lines) simulated by CICE5 is smoother and the region that shows the largest variability over the Barents–Kara Sea is located more southward compared to observations and PIOMAS. This could result from the missing ocean dynamics in CICE5. The difference of simulated sea ice between the two sea ice models could also result from what reanalysis product is used (Notz et al. 2013; Lindsay et al. 2014; Lee et al. 2019).

b. *Methods to identify high-latitude circulation patterns*

We use SOM analysis, a machine-learning clustering tool, to partition atmospheric circulation according to pattern similarity. The SOM algorithm assigns the circulation field on each day to a best-matching cluster by minimizing the Euclidean distance. After each assignment, the best-matching cluster and its neighboring clusters are adjusted by the new data weighted by the neighborhood function, in which the best-matching cluster has the greatest weight and other neighboring clusters have a smaller weight based on their distance from the best-matching cluster. These two procedures iterate many times to ensure that the assignment becomes stable. Owing to the neighborhood function in the SOM algorithm, the clusters "self-organize" such that similar clusters are located close together and dissimilar clusters are located farther apart on the SOM map. The topological ordering in SOM allows an effective visualization of a continuum of circulation patterns (Johnson et al. 2008; Johnson and Feldstein 2010). The SOM analysis has demonstrated a strong capability to partition meaningful patterns in many studies, including those focusing on the Arctic atmosphere (e.g., Cassano et al. 2006; Skific et al. 2009; Nygård et al. 2019) and Arctic sea ice (e.g., Mills and Walsh 2014; Yu et al. 2019; Horvath et al. 2021; Yu et al. 2021). For a full description of the SOM algorithm, readers are referred to Kohonen (1982), Kohonen (2012), and the appendix of Johnson et al. (2008).

For our study, we use December–March daily 500-hPa geopotential height anomaly fields with a 1° × 1° resolution over the Euro-Atlantic sector (60°E–90°W) in high latitudes (60°–90°N). We calculate anomalies by subtracting the seasonal cycle (climatological daily mean smoothed by a 31-day running average). We also remove the long-term linear trend at each grid point to focus on the short-term fluctuations. We weight the data by the square root of cosine of latitude to account for the increasing grid density with latitudes (Johnson and Feldstein 2010; Lee et al. 2011) before applying the SOM algorithm. We use a Python package "somoclu" version 1.75 (Wittek et al. 2013) to perform the SOM algorithm. The Python script to run the SOM algorithm and some predefined parameters (e.g., epochs, learning rate, radius of the neighborhood functions) are available online (see the data availability statement at the end of the article). The most important parameter that has to be specified is the SOM map size, which determines the number of clusters and the number of neighbors of each cluster.

We choose the 3 × 3 SOM map size by considering three measures: similarity within and between clusters (Johnson 2013; Lee and Kim 2019) and reproducibility (Bao and Wallace 2015). We calculate pattern correlations to quantify the similarity within and between clusters (Fig. S1a in the online supplemental material). When the number of clusters increases, more spatial details of the circulation fields can be resolved and classified, and hence the pattern similarity within a cluster increases (blue line). However, the patterns of different clusters would become less distinguishable (red line). An optimal map size should be large enough to capture the intracluster similarity while small enough to keep intercluster distinguishable. Hence, the intersection between the two lines (gray shading in Fig. S1a; 8–11 SOM patterns) is optimal. To test which map size within this range yields the most reproducible SOM patterns, we run the SOM in all possible map sizes (8 × 1, 4 × 2, 3 × 3, 9 × 1, 10 × 1, 5 × 2, 11 × 1) for 20 different realizations with random initialization. We calculate pattern correlations between members to quantify the reproducibility. We find that the 3 × 3 map size is highly reproducible (Fig. S1b). In the following, we present the SOM patterns from a member that shows high pattern correlations with most others. Using pattern correlations as a measure shows that this set of SOM clusters can well represent the spatial pattern of their members (Fig. S2).

c. *Methods to quantify the strength of the circulation patterns*

The anomalous circulation field on each day is assigned to one of the nine clusters according to pattern similarity but not the strength of the atmospheric flow. To quantify the strength, we spatially project the weighted daily circulation fields ($\mathbf{Z}_{\text{daily}}$) onto their assigned clusters' centroids ($\mathbf{Z}_{\text{centroid}}$) for a domain of 60°–90°N, 60°E–90°W:

$$\beta = \mathbf{Z}_{\text{daily}} \cdot \mathbf{Z}_{\text{centroid}}, \tag{1}$$

where β is the strength of the circulation pattern, and $\mathbf{Z}_{\text{daily}}$ and $\mathbf{Z}_{\text{centroid}}$ are in vector forms; $\mathbf{Z}_{\text{centroid}}$ is defined as the average of the daily circulation fields assigned to that cluster (as shown in Fig. 2 contours). The β within a cluster is then normalized between 0 and 1 to represent the relative strength.

d. *Methods to define sea ice changes and their relationship with SOM patterns*

To investigate daily relationships between circulation patterns and sea ice changes, we composite daily sea ice concentration and thickness changes on individual SOM clusters. We also calculate the correlations between the strength of the circulation patterns and daily sea ice changes. A two-tailed t test is used for significance testing. The daily sea ice changes on day n is defined as

$$\Delta A(n) = \frac{A(n+1) - A(n-1)}{2}, \tag{2}$$

where A is sea ice concentration or thickness. The sea ice changes in Eq. (2) spans a 3-day period centered on day n (Yang and Magnusdottir 2017). Using sea ice changes spanning

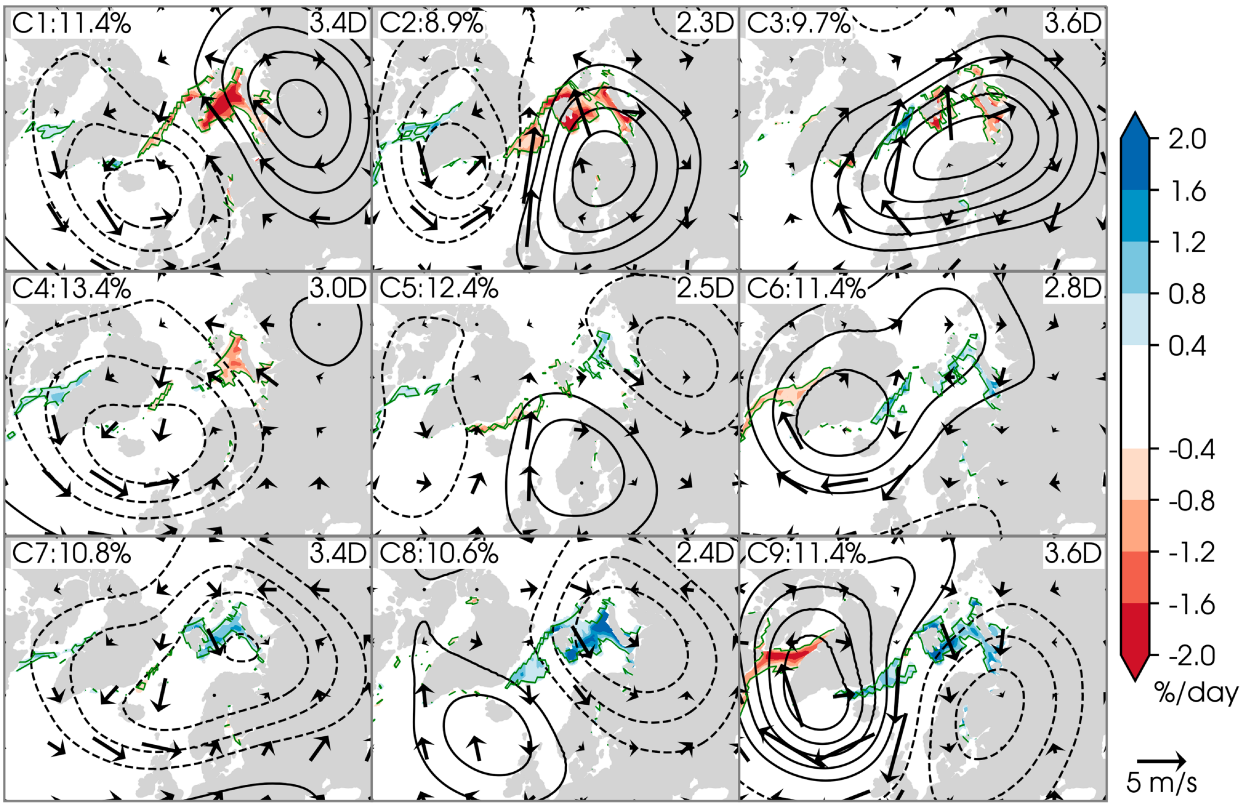

FIG. 2. Linkages between SOM circulation patterns and daily sea ice changes. Composites of anomalous 500-hPa geopotential height (black contours at 40-m intervals $\geq |40|$ m; dashed contours indicate negative values), 10-m zonal and meridional winds (black vectors), and NSIDC satellite daily sea ice concentration changes (shading; significant values at the 5% level are enclosed by green contours) for SOM clusters C1–C9. Numbers in the top-left corners of panels indicate the cluster number and frequency of occurrence. Numbers in the top-right corners indicate the average duration days of the cluster [following Falkena et al. (2020)].

a 5-day period (Wang et al. 2020; Clancy et al. 2022) produces similar results.

To further investigate the relationships between circulation patterns and sea ice changes from synoptic to submonthly time scales, we calculate the correlations between how long the ice-loss-favoring (or ice-growth-favoring) patterns persist and the summation of daily sea ice changes over the persistent period. For their relationships on seasonal time scales, we calculate the interannual correlations between a seasonal circulation index and the winter-mean (DJFM) Barents–Kara sea ice concentration as well as its growth (i.e., summation of daily sea ice changes over the whole season). The seasonal circulation index in each winter is defined as the frequency of ice-growth-favoring patterns minus the frequency of ice-loss-favoring patterns. The significance is tested by calculating similar correlations but with randomly reshuffled circulation clusters for all winter days for 10 000 times.

e. *Methods to investigate the physical mechanisms*

The atmospheric circulation influences sea ice via thermodynamic and dynamic pathways, in which sea ice concentration and thickness changes can be decomposed into dynamic and thermodynamic components. The dynamic component is the sea ice changes due to ice advection and convergence. The thermodynamic component is the sea ice changes due to heat transfer via radiation and conduction. The evolution of sea ice concentration or thicknesses is

$$\frac{dA}{dt} = -\nabla \cdot (\mathbf{u}_i A) + s, \tag{3}$$

where A can be sea ice concentration or thickness, $\mathbf{u}_i$ is the ice drift, and s is changes associated with thermodynamic processes that are not directly linked to sea ice motion (Holland and Kwok 2012; Park et al. 2015; Park and Stewart 2016; Cai et al. 2020). Thus, terms from left to right in Eq. (3) are total sea ice tendency, dynamic sea ice tendency, and thermodynamic sea ice tendency. For sea ice concentration, there is an additional term Ψ representing deformation in the dynamic tendency. The sea ice models explicitly simulate and output the total, dynamic, and thermodynamic tendencies as diagnostics. Note that the sea ice models define sea ice thickness as the sea ice volume per unit area (i.e., effective sea ice thickness).

We also use the following atmospheric variables to investigate the thermodynamic pathways: temperature at 850 hPa (T_{850}), horizontal temperature advection at 850 hPa ($\mathbf{u}_{850}\nabla T_{850}$, where $\mathbf{u}_{850}$ is the horizontal vector winds at 850 hPa), column moisture

(Q), column moisture convergence ($-\nabla \cdot \int_0^{1000\text{hPa}} \mathbf{u}_p q_p \, dp$, where $\mathbf{u}_p$ is the horizontal vector wind and q_p is the specific humidity both at pressure level p), and surface energy fluxes (surface sensible heat flux, surface latent heat flux and downward longwave radiation). We use the following atmospheric variables to investigate the dynamic pathways: 10-m zonal and meridional winds. For all variables, we remove the seasonal cycle and long-term trends to obtain the anomalies.

Last, we use partial correlations to test the relationships between the seasonal circulation index and the two physical processes (thermodynamics and dynamics) contributing to the Barents–Kara sea ice seasonal growth. The relationships between the circulation and the two physical processes obtained by the ordinary correlation test might be masked by the highly dependent dynamic and thermodynamic processes. The partial correlation helps reveal the true relationship by calculating the linear relationship between two variables x (circulation index) and y (e.g., thermodynamic ice changes) while taking away the effect of another variable z (e.g., dynamic ice changes). The notation is

$$\rho(x, y \mid z) = \frac{r_{xy} - r_{xz} r_{yz}}{\sqrt{1 - r_{xz}^2}\sqrt{1 - r_{yz}^2}}, \tag{4}$$

where r_{xy} is the Pearson correlation between x and y and so on.

3. Results

a. *High-latitude circulation patterns and day-to-day sea ice changes*

The SOM method reveals nine high-latitude circulation patterns in the cold season over the satellite period (Fig. 2, contours). All these circulation patterns show unique large-scale flow from 500 hPa (contours) down to the surface (vectors). The SOM method also provides information on the temporal variability of the circulation patterns. The information includes the frequency of occurrence (8.9%–13.4%, upper-left corners of individual panels) and average duration days (2.3–3.6 days, upper-right corners). In a few rare events one pattern can persist for more than 10 days (Fig. S3). The role of the circulation's persistence on sea ice changes over longer time scales will be explored in section 3c. Here, we first explore the day-to-day relationships between the circulation patterns and sea ice changes using a composite approach (i.e., averaging the daily observed sea ice changes across all days within the individual clusters).

All circulation patterns favor daily sea ice loss or growth to various extents, with a few patterns exerting a larger impact. The color shadings in Fig. 2 are observed daily sea ice concentration changes for each SOM pattern. The first four circulation patterns (C1–C4) favor sea ice concentration loss over sea ice basins in the North Atlantic. Among them, patterns C1 and C2 show the strongest sea ice loss over the Barents, Kara, and Greenland Seas. The C2 pattern, with a high pressure center over Scandinavia and a low pressure center over Greenland, resembles the typical circulation pattern that is found to drive significant Barents–Kara sea ice loss (Woods and Caballero 2016; Luo et al. 2017; Yang and Magnusdottir 2017; Zheng et al. 2022). The C1 pattern, with a high pressure center over Urals and a low pressure center over Iceland, also shows significant sea ice reduction, but has received less attention. The C3 pattern, resembling the Scandinavian–Ural blocking episodes evident by relatively long duration days (3.6 days on average), also favor Barents–Kara sea ice loss (e.g., Tyrlis et al. 2019; Chen et al. 2018). The C4 pattern resembles the positive phase of the North Atlantic Oscillation (NAO) with low pressure over the subpolar North Atlantic and a positive center in Azores (visible from a bigger map). The NAO's effect on the North Atlantic sea ice reduction has been noted before on subseasonal to seasonal time scales (Fang and Wallace 1994; Deser et al. 2000). The remaining circulation patterns, C6, C7, C8, and C9, appear to be the opposite-phase counterparts of C4, C3, C1, and C2 respectively. As expected, these patterns tend to favor sea ice growth, with patterns C8 and C9 being more prominent. Overall, the SOM analysis successfully identifies the important circulation patterns that are associated with the North Atlantic sea ice changes over weather time scales.

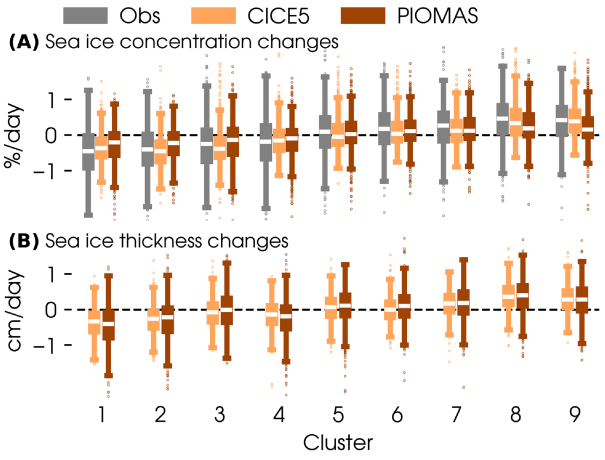

FIG. 3. A summary of observed and simulated Barents–Kara sea ice changes in individual clusters. Boxplots indicate anomalous daily Barents–Kara sea ice (a) concentration and (b) thickness changes from NSIDC satellite observations (gray), sea ice models CICE5 (orange), and PIOMAS (brown) for individual clusters. The boxes indicate the 25th and 75th percentiles, whiskers indicate the 1st and 99th percentiles, and dots indicate outliers.

Sea ice models (CICE5 and PIOMAS) forced by observed atmospheric conditions can largely reproduce the circulation–ice relationships. Figure 3a summarizes observed (gray boxplots) and simulated (orange boxplots for CICE5 and brown boxplots for PIOMAS) Barents–Kara sea ice (65°–85°N, 10°–100°E) concentration changes for each circulation cluster. The sea ice models and observations show the same sign of sea ice changes for each pattern, although models tend to simulate a smaller spread. The models agree with observations that patterns C1 and C2 (C8 and C9; their opposite-phase counterparts) yield the strongest sea ice reduction (growth). Approximately three-quarters of winter days assigned to these clusters show

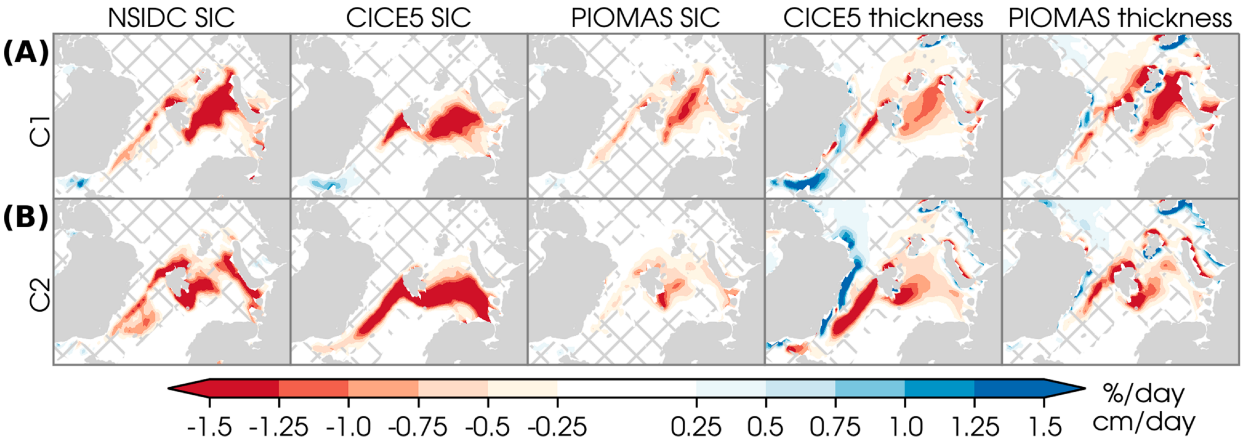

FIG. 4. Composites of anomalous daily sea ice changes (shading)—(from left to right) NSIDC satellite sea ice concentration, CICE5 simulated sea ice concentration, PIOMAS simulated sea ice concentration, CICE5 simulated sea ice thickness, and PIOMAS simulated sea ice thickness, respectively—for clusters (a) C1 and (b) C2. Hatching indicates insignificant values at the 5% level using a two-tailed t test.

negative (positive) observed or simulated sea ice concentration changes. The two models also broadly reproduce the spatial patterns of observed sea ice concentration changes (Fig. 4 for patterns C1 and C2 and Fig. S4 for patterns C8 and C9), although PIOMAS tends to underestimate the amplitude. Sea ice thickness shows the same sign of changes as sea ice concentration for most clusters (Figs. 3b). Similar to sea ice concentration changes, the largest thickness loss (growth) is found for patterns C1 and C2 (C8 and C9). In the models sea ice thickness is defined as the average sea ice volume per unit area, and hence the results for sea ice thickness can similarly apply for sea ice volume.

Daily circulation fields assigned to the same cluster share the pattern similarity but not the strength of the atmospheric flow, which could partly explain the large spread of sea ice changes shown in Fig. 3. To obtain indices that represent the strength of the atmospheric flow, we project the daily circulation fields onto the assigned clusters (see section 2), and then relate such indices with daily Barents–Kara sea ice changes. Using pattern C1 as an example, the circulation strength is significantly correlated with both observed and simulated sea ice concentration ($\rho = -0.37$ to -0.42; Fig. 5a) and simulated thickness ($\rho = -0.4$ to -0.47; Fig. 5b) changes. We also find similar relationships for other clusters (Fig. 5c). The circulation–ice relationships identified from the correlation analyses are generally consistent with the results from the composite analyses (as in Figs. 2 and 3). Other than the strength of the circulation pattern, we find that the initial sea ice state also plays a role to explain the spread, but generally weaker (Fig. S5).

b. *Underlying mechanisms: Dynamic and thermodynamic pathways*

Since the sea ice models forced by observed surface fields successfully reproduce observed sea ice changes, we further use the models to assess the relative contributions from the thermodynamic and dynamic processes to sea ice changes (see section 2). Thermodynamic ice changes are sea ice melting or freezing largely resulting from atmospheric surface temperature, moisture, and wind speed fluctuations that perturb the surface energy budget. Dynamic ice changes are sea ice mechanical redistribution resulting from wind-driven ice advection and convergence. We will present the results of the decomposition from CICE5, which better reproduces the amplitude of observed sea ice concentration changes (shown in Figs. 3 and 4). Further, CICE5 is coupled with a slab-ocean model without ocean dynamics, hence isolating the atmospheric-driven sea ice variability that is the focus of this study. We will also focus on the circulation patterns C1 and C2 that produce the strongest sea ice reduction. Relevant results from other patterns are shown as supplemental figures.

Although recent studies have highlighted the thermodynamic processes contributing to the Barents–Kara sea ice loss on synoptic time scales (e.g., Park et al. 2015; Wang et al. 2020; Zheng et al. 2022), our results show that wind-driven dynamic processes contribute comparably or even more. Figure 6 shows the anomalous sea ice concentration and thickness changes resulting from thermodynamic and dynamic processes. For both patterns C1 and C2, thermodynamic and dynamic processes contribute comparably in magnitude to sea ice concentration loss over the Greenland and Barents–Kara Seas (first two columns in Fig. 6). In contrast, dynamic processes dominate the sea ice thickness or volume changes everywhere (last two columns) associated with anomalous sea ice motions (vectors). Overall, these results suggest that dynamic processes are more effective than thermodynamic processes in reducing the Barents–Kara sea ice layers by pushing sea ice northward. Thermodynamic processes are only able to melt or freeze the ice cover layer near the sea ice edge where the sea ice is thin. The dominant role of dynamic processes on sea ice thickness changes also applies to other circulation patterns and another sea ice model PIOMAS (Figs. S6 and S7).

The atmospheric circulation plays an important role in modulating the anomalous sea ice motions and hence the dynamic sea ice changes. Pattern C1 shows an anomalous cyclonic ice motion over Svalbard (Fig. 6a, vectors) that is consistent with the overlying cyclonic circulation (Fig. 2, vectors). Such cyclonic ice drifts result in sea ice concentration and thickness reduction over the Barents–Kara Sea and sea ice production along the Denmark

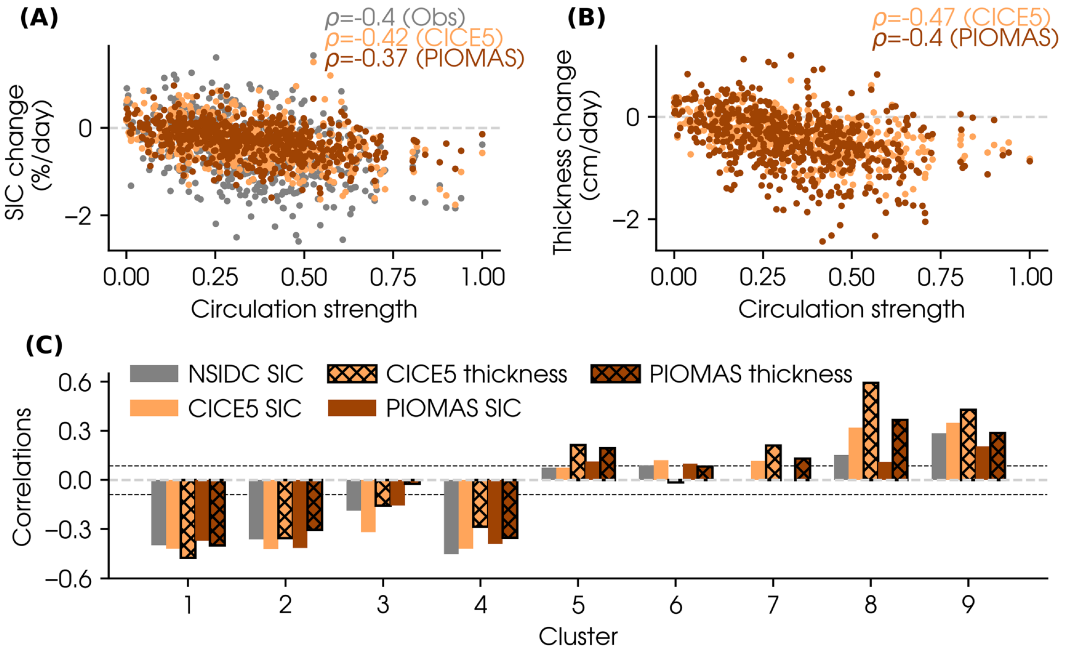

FIG. 5. Relationships between the strength of the circulation pattern and daily Barents–Kara sea ice (a) concentration and (b) thickness changes from NSIDC satellite observations (gray), sea ice models CICE5 (orange), and PIOMAS (brown) for cluster C1. (c) Correlations between the strength of the circulation pattern and daily Barents–Kara sea ice changes—from left to right: gray for NSIDC observed sea ice concentration, orange for CICE5 sea ice concentration, hatched orange for CICE5 sea ice thickness, brown for PIOMAS sea ice concentration, and hatched brown for PIOMAS sea ice thickness, respectively—for individual clusters. Horizontal lines show the significance threshold at the 5% level using a two-tailed t test for a sample size of 500 (similar to the sample size for each cluster).

Strait mostly via sea ice advection (the advection is dominated by anomalous ice drifts along the climatological thickness gradient; see Fig. S8a for details). Instead, pattern C2 shows relatively strong anomalous poleward ice drifts over the Atlantic sea ice basins (Fig. 6b, vectors) consistent with the overlying circulation. The winds mechanically push the sea ice northward, which is redistributed as ice growth near the northern and northeast Greenland coastlines (Fig. 6b, third column) mostly via sea ice convergence (Fig. S8b). Some sea ice is even redistributed to remote Canada basins (Figs. S6 and S7 show a bigger map to confirm this).

Although thermodynamic processes seem to be secondary on synoptic time scales, they are still effective in melting or freezing the top layer of sea ice. The thermodynamic processes leading to sea ice changes are also strongly linked to the atmospheric circulation. While both patterns C1 and C2 favor southerly flow that brings low-latitude air masses toward the ice-covered region, these air masses originate from different sectors. Pattern C1 brings continental air from Scandinavia and the Urals, which is warmer and moister than air over the Barents–Kara Sea, but is still relatively cooler and drier compared to marine air masses advected by pattern C2 (see the circulation flow shown by Fig. 2 and the climatology of low-level temperature and moisture in Fig. S9). As a result, the temperature advection from pattern C1 is weak and mostly located in the Barents–Kara Sea and Taymyr Peninsula, and the moisture convergence is weak everywhere (Fig. 7a; first two columns). By contrast, temperature advection and moisture convergence from pattern C2 are stronger and concentrated over the ocean basins including the Norwegian, Greenland, and Barents Seas (Fig. 7b; first two columns). The differences in heat and moisture advection largely explain the difference in low-level atmospheric temperature (third column), column moisture (fourth column), and surface energy fluxes (Fig. 8) for these two patterns.

The anomalous downward surface energy fluxes can be further decomposed into sensible, latent, and downward longwave radiation. Sensible heat flux dominates as compared to latent heat flux and downward longwave radiation near the sea ice edge and over the ocean, seen in both patterns C1 and C2 (Fig. 8). The downward longwave radiation driven by enhanced moisture and temperature extends farther northward and eastward and covers a large area of the sea ice region. These surface downward fluxes collectively contribute to melting of the sea ice concentration and a small part of thickness changes (Fig. 6, second and fourth columns). Pattern C2 shows an elongated sea ice melting in the Greenland sea ice edge consistent with the strong downward fluxes there (Fig. 8b). The thermodynamic pathways in driving sea ice concentration growth for patterns C8 and C9 are similar to C1 and C2, but with opposite signs (not shown).

c. *Persistence of circulation patterns sets up seasonal circulation–ice linkages*

The results to this point highlight the synoptic linkages between the circulation patterns and sea ice changes. However,

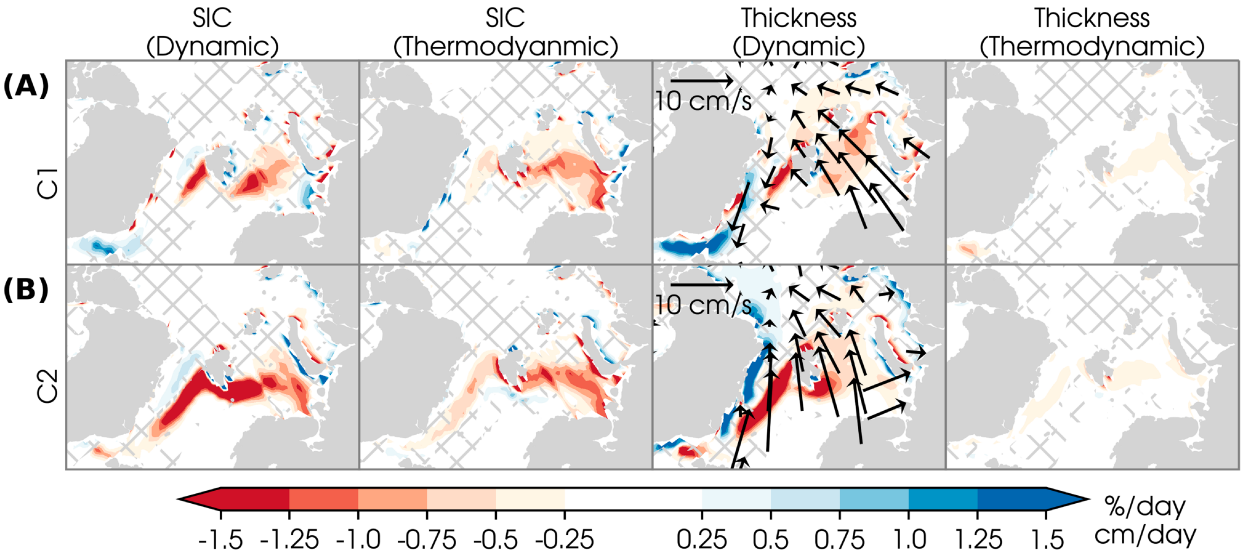

FIG. 6. Composites of anomalous daily sea ice changes from sea ice model CICE5 (shading)—(from left to right) dynamic sea ice concentration changes, thermodynamic sea ice concentration changes, dynamic sea ice thickness changes, and thermodynamic sea ice thickness changes, respectively—for clusters (a) C1 and (b) C2. Hatching indicates insignificant shading values at the 5% level using a two-tailed t test. Vectors in the third column indicate the anomalous sea ice drifts. The sum of dynamic and thermodynamic components equal to the total sea ice concentration or thickness changes from CICE5 shown in Fig. 4.

sea ice changes over monthly and seasonal time scales have received more attention since they can have larger local and remote climate impacts (Cohen et al. 2014; Wu and Smith 2016; Zhang et al. 2018; Siew et al. 2020). We further investigate the circulation–ice linkages on longer time scales by accounting for the persistence of circulation patterns.

Results show that when a circulation pattern persists, sea ice loss or growth tends to last longer and ends up larger. Figure 9a shows a negative relationship ($\rho = -0.52$; bootstrapped samples of random days without any preferred pattern result in null correlations) between the accumulated Barents–Kara sea ice concentration changes and how long the ice-loss-

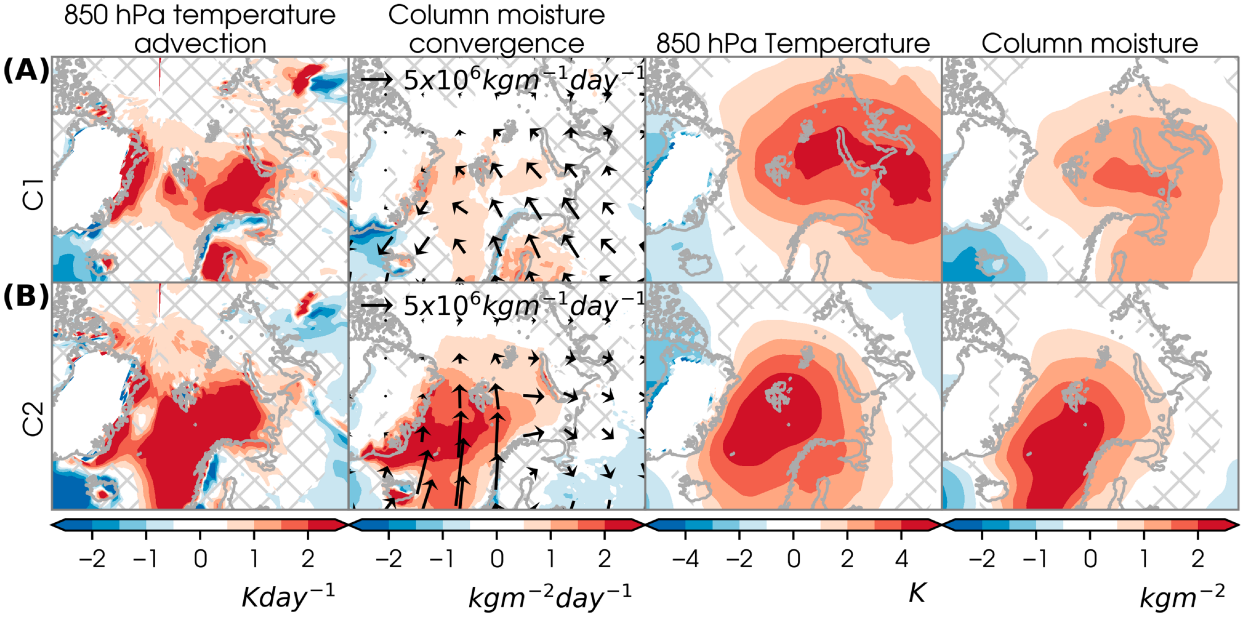

FIG. 7. Composites of variables related to atmospheric heat and moisture transports (shading) —(from left to right) anomalous 850-hPa temperature advection, column moisture convergence, 850-hPa temperature, and column moisture, respectively—for clusters (a) C1 and (b) C2. Hatching indicates insignificant shading values at the 5% level using a two-tailed t test. Vectors in the second column indicate the zonal and meridional column moisture fluxes.

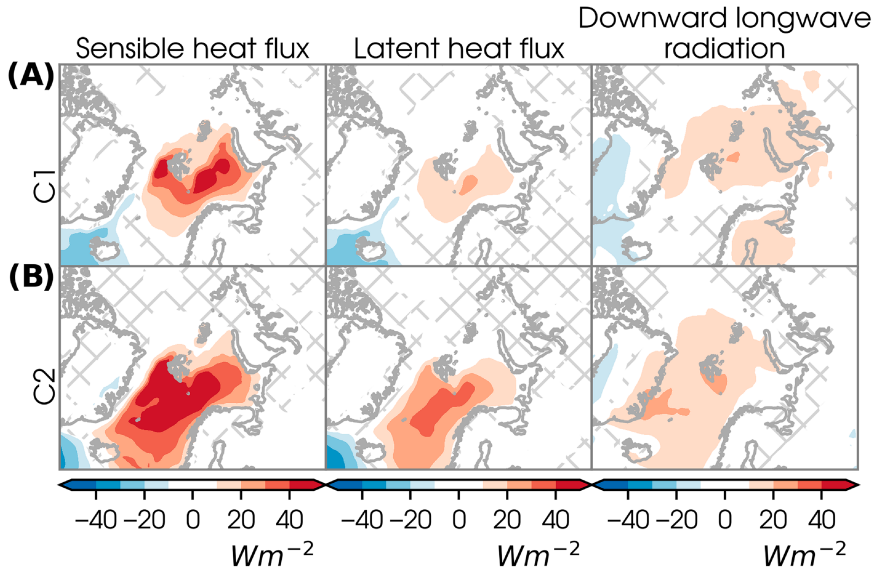

FIG. 8. Composites of anomalous surface energy fluxes (shading)—(from left to right) sensible heat flux, latent heat flux, and downward longwave radiation, respectively—for clusters (a) C1 and (b) C2. Hatching indicates insignificant values at the 5% level using a two-tailed t test. Heat fluxes from the atmosphere to the ocean are defined as positive.

favoring patterns (C1–C4) persist. Day-to-day sea ice changes are usually small; however, when these circulation patterns persist, the daily sea ice loss can accumulate up to −15% in a few extreme events with long persistence. Likewise, a positive relationship (ρ = 0.49) is found for ice-growth-favoring patterns (C6–C9, Fig. 9b). We also find similar results if we account for sea ice thickness rather than sea ice concentration (not shown).

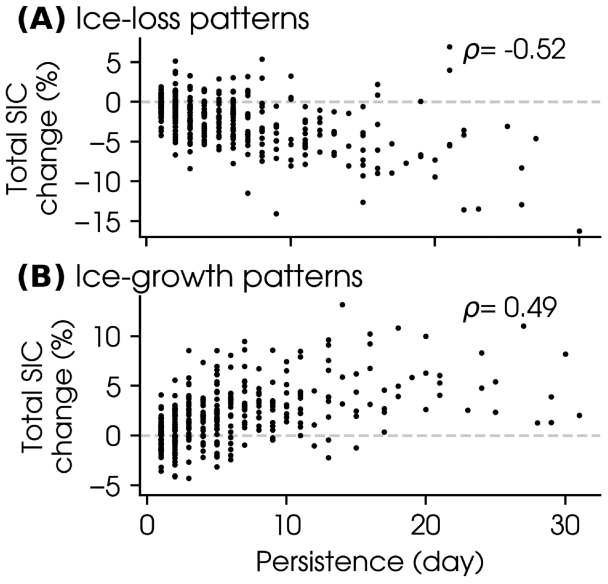

FIG. 9. Relationships between accumulation of daily Barents–Kara sea ice concentration changes and persistent days of (a) ice-loss-favoring (C1–C4) and (b) ice-growth-favoring (C6–C9) circulation patterns. These correlations are significant at the 5% level using a bootstrapping test.

In terms of seasonal sea ice changes, it is more relevant to ask if more frequent ice-loss (ice-growth)-favoring patterns during the winter season December–March (DJFM) lead to more sea ice loss (growth).

We first count the total number of days with ice-loss-favoring patterns (C1–C4; red bars in Fig. 10) and ice-growth-favoring patterns (C6–C9; blue bars) in each winter (DJFM) season. A seasonal circulation index is then defined as the difference between them (gray solid line). A winter with more ice-growth patterns than ice-loss patterns has a positive index, and vice versa. We then correlate this circulation index with DJFM seasonal-mean sea ice concentration (black solid line) and the sea ice growth (by summing the daily sea ice concentration changes from 1 December to 31 March). Significant correlations are found between the circulation index and winter sea ice concentration as well as the sea ice growth (ρ = 0.54 and 0.5 respectively). These results indicate that the persistence of daily atmospheric circulation patterns can help set up seasonal sea ice variability, consistent with previous studies (Wernli and Papritz 2018; Wang et al. 2020).

This exercise also allows us to explore the role of dynamic versus thermodynamic processes on seasonal time scales. Figure 11 shows wintertime Barents–Kara sea ice concentration growth anomalies (the same sea ice growth as in Fig. 10 but removing the climatological mean) for observations (dotted line) and the model CICE5 (solid line). CICE5 can well capture the observed seasonal sea ice growth, which is further decomposed into dynamic (blue bars) and thermodynamic (orange bars) components. The seasonal circulation index (gray line in Fig. 10) is only weakly correlated with the seasonal thermodynamic and dynamic components (ρ = 0.11 and 0.36, respectively). Such weak correlations could be masked by the strong interaction and cancelling between the two processes in the ice growth seasons, evident by

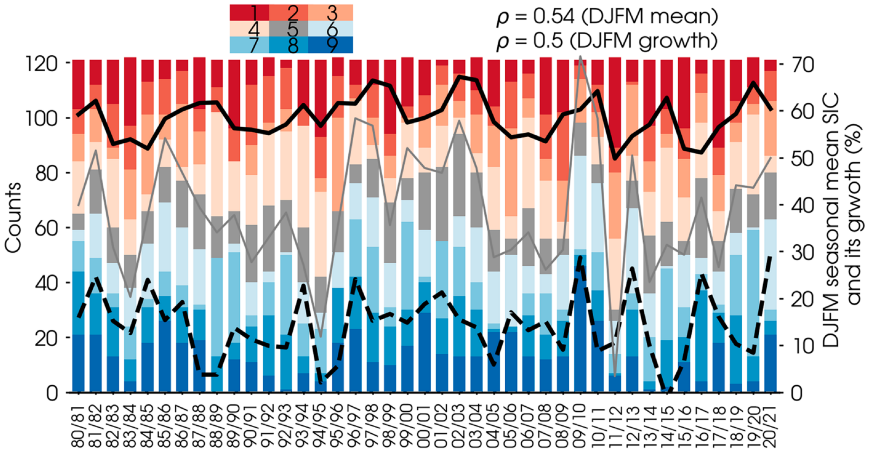

FIG. 10. Frequency of circulation patterns partially explains seasonal sea ice concentration changes. Bars indicate the frequency of individual clusters in winters (December–March) from 1980/81 to 2020/21. Red bars indicate ice-loss-favoring patterns (C1–C4) and blue bars indicate ice-growth-favoring patterns (C6–C9) patterns. Gray solid line indicates the circulation index (the difference between red and blue bars). The axis label for the gray line is not shown. Black lines indicate NSIDC observed DJFM-mean Barents–Kara sea ice concentration (solid line) and its growth (dashed line). The correlations in the top-right corners indicate the relationships between the circulation index and DJFM-mean sea ice concentration (DJFM mean) and between the circulation index and DJFM sea ice growth (DJFM growth). These correlations are significant at the 5% level using a bootstrapping test.

their negative relationships ($\rho = -0.52$). We can use partial correlations to isolate the relationship between the circulation index and thermodynamic (dynamic) processes by removing the effect of dynamic (thermodynamic) processes. Such an exercise shows that the circulation index is more effectively linked to thermodynamic and dynamic processes ($\rho = 0.37$ and 0.49, respectively). However, the total seasonal sea ice anomalies covary with the thermodynamic ($\rho = 0.71$) more than the dynamic ($\rho = 0.24$) components, indicating a stronger role of thermodynamic processes in modulating the sea ice concentration on the seasonal time scale. Together this evidence suggests that some other processes not directly linked to the circulation modulate the seasonal sea ice via thermodynamic processes (see section 4).

4. Conclusions and discussion

Our study investigates the mechanistic links from high-latitude atmospheric circulation patterns to wintertime Barents–Kara sea ice variability from synoptic to seasonal time scales over the satellite era. We identify nine circulation patterns that are important for sea ice loss and growth. Some circulation patterns are consistent with previous findings. Two circulation patterns, with a high pressure center over the Urals (Scandinavia) and a low

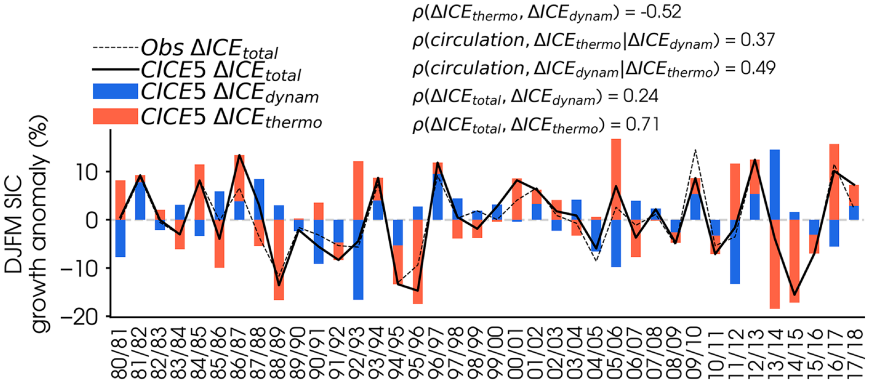

FIG. 11. Thermodynamic and dynamic processes contributing to wintertime (DJFM) Barents–Kara sea ice concentration growth from 1980/81 to 2017/18. Black lines show the anomalous Barents–Kara sea ice concentration growth in winter from NSIDC satellite observations (dotted line) and sea ice model CICE5 (solid line). Sea ice concentration growth from CICE5 is further decomposed into thermodynamic (orange bars) and dynamics (blue bars) changes.

pressure center over Iceland (Greenland), are found to be the most important for day-to-day Barents–Kara sea ice loss. Accounting for the persistence of these synoptic circulation patterns helps explain sea ice variability from synoptic to seasonal time scales. Our study also provides new insights into the physical mechanisms responsible for sea ice changes by using sea ice models that isolate thermodynamic and dynamic processes. While previous studies emphasize the role of thermodynamic processes (e.g., enhanced moisture transport and downward longwave radiation), we highlight that wind-driven dynamic processes are as important as thermodynamic processes for Barents–Kara sea ice concentration changes, and even dominate the thickness or volume changes on synoptic time scales. On seasonal time scales, thermodynamic processes seem to play a stronger role than dynamic processes.

Although circulation–ice linkages appear to be robust, the correlations between the circulation indices and sea ice changes are only moderate (about 0.4–0.6) across synoptic to seasonal time scales. These moderate correlations suggest that other processes also play roles to modulate Barents–Kara sea ice variability. Some of these can be regarded as second-order processes that lag the heat and moisture advection by the circulation (Nygård et al. 2021), including the formation of clouds, snowfall on sea ice, local radiative cooling, and Arctic surface warming modulated by sea ice loss (e.g., Liu and Key 2014; Kim and Kim 2017; Pithan et al. 2018; Webster et al. 2019). These processes can modify the air temperature and moisture profiles in the Arctic, and hence Arctic sea ice variability via thermodynamic forcing. The role of snowfall on sea ice is particularly complex in the cold season, which can both hinder sea ice growth by insulating the sea ice and ocean from the atmosphere (Maykut 1978; Lim et al. 2022b) and enhance sea ice thickness growth via snow and ice formation (Granskog et al. 2017; Webster et al. 2018; Merkouriadi et al. 2020). Other non-atmospheric processes including the preconditioning of sea ice concentration and thickness and oceanic heat transport (e.g., Årthun et al. 2012; Singh et al. 2017; Dörr et al. 2021) could also modulate how the circulation–ice relationships manifest.

The moderate circulation–ice relationships could also arise from the fact that the relationships have been nonstationary over past few decades in a warming climate. In a warming climate, the sea ice has become thinner and more mobile, and its edge has shifted northward. The negative feedback that controls thinner sea ice growing faster in the cold season seems to have experienced changes (Petty et al. 2018; Stroeve et al. 2018). All these changing processes have potential to interfere with the circulation–ice relationships operating on shorter time scales and make the relationships nonstationary. A few studies show that the thinner sea ice has been more vulnerable to atmospheric forcing in the past decades (e.g., Kwok 2018; Aue et al. 2022; Rheinlænder et al. 2022). Nevertheless, detecting robust changes of the circulation–ice relationships is challenging when the satellite observational record is still short (about 40 years). A more comprehensive study using climate models forced by different extents of anthropogenic forcing (e.g., preindustrial, historical, and future emissions scenarios) is required to detect robust changes (e.g., Holland and Stroeve 2011; Petty et al. 2018).

Another remaining question is to identify robust precursors that favor the persistence of circulation patterns and hence long-lasting sea ice changes. Possible precursors that can provide sources of predictability in weeks to months include the Madden–Julian oscillation (Henderson et al. 2014; Park et al. 2015; Zheng et al. 2022; Jiang et al. 2021), El Niño–Southern Oscillation (Clancy et al. 2021; Luo et al. 2023), stratospheric (Smith et al. 2018), and Eurasian snow cover variability (Matsumura et al. 2014; Gastineau et al. 2017; Wegmann et al. 2021). Our study, along with previous and future studies that identify the precursors, will have important implications on improving seasonal Arctic sea ice prediction and understanding the sea ice decline over the past and future decades.

Acknowledgments. We thank Axel Schweiger and Jinlun Zhang for providing the daily PIOMAS data. We thank Jaewon Lee, Sarah Smith, Samuel Bartusek, and Yujia You for their useful discussion. We acknowledge the support from NASA Award 80NSSC20K1254. The authors declare that they have no conflicts of interests.

Data availability statement. MERRA-2 data are available through https://gmao.gsfc.nasa.gov/reanalysis/MERRA-2/. The NSIDC Climate Data Record of Passive Microwave Sea Ice Concentration, version 4, is available through https://nsidc.org/data/g02202/versions/4. CICE5 and PIOMAS model outputs are available upon request. The Python script including specified parameters to run the SOM algorithm, and the codes to generate all the plots are provided at https://github.com/PeterSiew/SiewEA2023_physical.

REFERENCES

Årthun, M., T. Eldevik, L. H. Smedsrud, Ø. Skagseth, and R. B. Ingvaldsen, 2012: Quantifying the influence of Atlantic heat on Barents Sea ice variability and retreat. *J. Climate*, **25**, 4736–4743, https://doi.org/10.1175/JCLI-D-11-00466.1.

Aue, L., T. Vihma, P. Uotila, and A. Rinke, 2022: New insights into cyclone impacts on sea ice in the Atlantic sector of the Arctic Ocean in winter. *Geophys. Res. Lett.*, **49**, e2022GL100051, https://doi.org/10.1029/2022GL100051.

Bailey, D., A. DuVivier, M. Holland, E. Hunke, B. Lipscomb, B. Briegleb, C. Bitz, and J. Schramm, 2018: CESM CICE5 users guide. National Center for Atmospheric Research, 51 pp., https://buildmedia.readthedocs.org/media/pdf/cesmcice/latest/cesmcice.pdf.

Bao, M., and J. M. Wallace, 2015: Cluster analysis of Northern Hemisphere wintertime 500-hpa flow regimes during 1920–2014. *J. Atmos. Sci.*, **72**, 3597–3608, https://doi.org/10.1175/JAS-D-15-0001.1.

Bintanja, R., and F. M. Selten, 2014: Future increases in Arctic precipitation linked to local evaporation and sea-ice retreat. *Nature*, **509**, 479–482, https://doi.org/10.1038/nature13259.

Boisvert, L. N., A. A. Petty, and J. C. Stroeve, 2016: The impact of the extreme winter 2015/16 Arctic cyclone on the Barents–Kara Seas. *Mon. Wea. Rev.*, **144**, 4279–4287, https://doi.org/10.1175/MWR-D-16-0234.1.

Cai, L., V. A. Alexeev, and J. E. Walsh, 2020: Arctic sea ice growth in response to synoptic-and large-scale atmospheric forcing from CMIP5 models. *J. Climate*, **33**, 6083–6099, https://doi.org/10.1175/JCLI-D-19-0326.1.

Cassano, E. N., A. H. Lynch, J. J. Cassano, and M. R. Koslow, 2006: Classification of synoptic patterns in the western Arctic associated with extreme events at Barrow, Alaska, USA. *Climate Res.*, **30**, 83–97, https://doi.org/10.3354/cr030083.

Chen, X., D. Luo, S. B. Feldstein, and S. Lee, 2018: Impact of winter Ural blocking on Arctic sea ice: Short-time variability. *J. Climate*, **31**, 2267–2282, https://doi.org/10.1175/JCLI-D-17-0194.1.

Clancy, R., C. Bitz, and E. Blanchard-Wrigglesworth, 2021: The influence of ENSO on Arctic sea ice in large ensembles and observations. *J. Climate*, **34**, 9585–9604, https://doi.org/10.1175/JCLI-D-20-0958.1.

——, ——, ——, M. C. McGraw, and S. M. Cavallo, 2022: A cyclone-centered perspective on the drivers of asymmetric patterns in the atmosphere and sea ice during Arctic cyclones. *J. Climate*, https://doi.org/10.1175/JCLI-D-21-0093.1, in press.

Cohen, J., and Coauthors, 2014: Recent Arctic amplification and extreme mid-latitude weather. *Nat. Geosci.*, **7**, 627–637, https://doi.org/10.1038/ngeo2234.

Deser, C., J. E. Walsh, and M. S. Timlin, 2000: Arctic sea ice variability in the context of recent atmospheric circulation trends. *J. Climate*, **13**, 617–633, https://doi.org/10.1175/1520-0442(2000)013<0617:ASIVIT>2.0.CO;2.

Ding, Q., and Coauthors, 2017: Influence of high-latitude atmospheric circulation changes on summertime Arctic sea ice. *Nat. Climate Change*, **7**, 289–295, https://doi.org/10.1038/nclimate3241.

Dörr, J., M. Årthun, T. Eldevik, and E. Madonna, 2021: Mechanisms of regional winter sea-ice variability in a warming Arctic. *J. Climate*, **34**, 8635–8653, https://doi.org/10.1175/JCLI-D-21-0149.1.

Falkena, S. K. J., J. de Wiljes, A. Weisheimer, and T. G. Shepherd, 2020: Revisiting the identification of wintertime atmospheric circulation regimes in the Euro-Atlantic sector. *Quart. J. Roy. Meteor. Soc.*, **146**, 2801–2814, https://doi.org/10.1002/qj.3818.

Fang, Z., and J. M. Wallace, 1994: Arctic sea ice variability on a timescale of weeks and its relation to atmospheric forcing. *J. Climate*, **7**, 1897–1914, https://doi.org/10.1175/1520-0442(1994)007<1897:ASIVOA>2.0.CO;2.

Finocchio, P. M., J. D. Doyle, and D. P. Stern, 2022: Accelerated sea ice loss from late summer cyclones in the new Arctic. *J. Climate*, **35**, 7751–7769, https://doi.org/10.1175/JCLI-D-22-0315.1.

Gastineau, G., J. García-Serrano, and C. Frankignoul, 2017: The influence of autumnal Eurasian snow cover on climate and its link with Arctic sea ice cover. *J. Climate*, **30**, 7599–7619, https://doi.org/10.1175/JCLI-D-16-0623.1.

Gelaro, R., and Coauthors, 2017: The Modern-Era Retrospective Analysis for Research and Applications, version 2 (MERRA-2). *J. Climate*, **30**, 5419–5454, https://doi.org/10.1175/JCLI-D-16-0758.1.

Gong, T., and D. Luo, 2017: Ural blocking as an amplifier of the Arctic sea ice decline in winter. *J. Climate*, **30**, 2639–2654, https://doi.org/10.1175/JCLI-D-16-0548.1.

Granskog, M. A., A. Rösel, P. A. Dodd, D. Divine, S. Gerland, T. Martma, and M. J. Leng, 2017: Snow contribution to first-year and second-year Arctic sea ice mass balance north of Svalbard. *J. Geophys. Res. Oceans*, **122**, 2539–2549, https://doi.org/10.1002/2016JC012398.

Hegyi, B. M., and P. C. Taylor, 2018: The unprecedented 2016–2017 Arctic sea ice growth season: The crucial role of atmospheric rivers and longwave fluxes. *Geophys. Res. Lett.*, **45**, 5204–5212, https://doi.org/10.1029/2017GL076717.

Henderson, G. R., B. S. Barrett, and D. M. Lafleur, 2014: Arctic sea ice and the Madden–Julian Oscillation (MJO). *Climate Dyn.*, **43**, 2185–2196, https://doi.org/10.1007/s00382-013-2043-y.

Hersbach, H., and Coauthors, 2020: The ERA5 global reanalysis. *Quart. J. Roy. Meteor. Soc.*, **146**, 1999–2049, https://doi.org/10.1002/qj.3803.

Holland, M. M., and J. Stroeve, 2011: Changing seasonal sea ice predictor relationships in a changing Arctic climate. *Geophys. Res. Lett.*, **38**, L18501, https://doi.org/10.1029/2011GL049303.

Holland, P. R., and R. Kwok, 2012: Wind-driven trends in Antarctic sea-ice drift. *Nat. Geosci.*, **5**, 872–875, https://doi.org/10.1038/ngeo1627.

——, and N. Kimura, 2016: Observed concentration budgets of Arctic and Antarctic sea ice. *J. Climate*, **29**, 5241–5249, https://doi.org/10.1175/JCLI-D-16-0121.1.

Horvath, S., J. Stroeve, B. Rajagopalan, and A. Jahn, 2021: Arctic Sea ice melt onset favored by an atmospheric pressure pattern reminiscent of the North American-Eurasian Arctic pattern. *Climate Dyn.*, **57**, 1771–1787, https://doi.org/10.1007/s00382-021-05776-y.

Jiang, Z., S. B. Feldstein, and S. Lee, 2021: Two atmospheric responses to winter sea ice decline over the Barents-Kara Seas. *Geophys. Res. Lett.*, **48**, e2020GL090288, https://doi.org/10.1029/2020GL090288.

Johnson, N. C., 2013: How many ENSO flavors can we distinguish? *J. Climate*, **26**, 4816–4827, https://doi.org/10.1175/JCLI-D-12-00649.1.

——, and S. B. Feldstein, 2010: The continuum of North Pacific sea level pressure patterns: Intraseasonal, interannual, and interdecadal variability. *J. Climate*, **23**, 851–867, https://doi.org/10.1175/2009JCLI3099.1.

——, ——, and B. Tremblay, 2008: The continuum of Northern Hemisphere teleconnection patterns and a description of the NAO shift with the use of self-organizing maps. *J. Climate*, **21**, 6354–6371, https://doi.org/10.1175/2008JCLI2380.1.

Jung, T., and M. Hilmer, 2001: The link between the North Atlantic Oscillation and Arctic sea ice export through Fram Strait. *J. Climate*, **14**, 3932–3943, https://doi.org/10.1175/1520-0442(2001)014<3932:TLBTNA>2.0.CO;2.

Kalnay, E., and Coauthors, 1996: The NCEP/NCAR 40-Year Reanalysis Project. *Bull. Amer. Meteor. Soc.*, **77**, 437–472, https://doi.org/10.1175/1520-0477(1996)077<0437:TNYRP>2.0.CO;2.

Kim, H.-M., and B.-M. Kim, 2017: Relative contributions of atmospheric energy transport and sea ice loss to the recent warm Arctic winter. *J. Climate*, **30**, 7441–7450, https://doi.org/10.1175/JCLI-D-17-0157.1.

Kobayashi, S., and Coauthors, 2015: The JRA-55 reanalysis: General specifications and basic characteristics. *J. Meteor. Soc. Japan*, **93**, 5–48, https://doi.org/10.2151/jmsj.2015-001.

Kohonen, T., 1982: Self-organized formation of topologically correct feature maps. *Biol. Cybern.*, **43**, 59–69, https://doi.org/10.1007/BF00337288.

——, 2012: *Self-Organizing Maps*. Springer Series in Information Sciences, Vol. 30, Springer, 502 pp.

Kopec, B. G., X. Feng, F. A. Michel, and E. S. Posmentier, 2016: Influence of sea ice on Arctic precipitation. *Proc. Natl. Acad. Sci. USA*, **113**, 46–51, https://doi.org/10.1073/pnas.1504633113.

Kostopoulos, D., E. Yitzhak, and O. T. Gudmestad, 2018: Coastal erosion due to decreased ice coverage, associated increased wave action, and permafrost melting. *Arctic Studies—A*

Proxy for Climate Change, IntechOpen, 25–35, https://doi.org/10.5772/intechopen.80604.

Kwok, R., 2018: Arctic sea ice thickness, volume, and multiyear ice coverage: Losses and coupled variability (1958–2018). *Environ. Res. Lett.*, **13**, 105005, https://doi.org/10.1088/1748-9326/aae3ec.

Lee, M.-H., and J.-H. Kim, 2019: The role of synoptic cyclones for the formation of Arctic summer circulation patterns as clustered by self-organizing maps. *Atmosphere*, **10**, 474, https://doi.org/10.3390/atmos10080474.

Lee, S., T. Gong, N. Johnson, S. B. Feldstein, and D. Pollard, 2011: On the possible link between tropical convection and the Northern Hemisphere Arctic surface air temperature change between 1958 and 2001. *J. Climate*, **24**, 4350–4367, https://doi.org/10.1175/2011JCLI4003.1.

Lee, S.-B., B.-M. Kim, J. Ukita, and J.-B. Ahn, 2019: Uncertainties in Arctic sea ice thickness associated with different atmospheric reanalysis datasets using the CICE5 model. *Atmosphere*, **10**, 361, https://doi.org/10.3390/atmos10070361.

Liang, X., X. Li, H. Bi, M. Losch, Y. Gao, F. Zhao, Z. Tian, and C. Liu, 2022: A comparison of factors that led to the extreme sea ice minima in the twenty-first century in the Arctic Ocean. *J. Climate*, **35**, 1249–1265, https://doi.org/10.1175/JCLI-D-21-0199.1.

Lim, W.-I., H.-S. Park, A. A. Petty, and K.-H. Seo, 2022a: The role of summer snowstorms on seasonal Arctic sea ice loss. *J. Geophys. Res. Oceans*, **127**, e2021JC018066, https://doi.org/10.1029/2021JC018066.

——, ——, A. L. Stewart, and K.-H. Seo, 2022b: Suppression of Arctic sea ice growth in the Eurasian–Pacific seas by winter clouds and snowfall. *J. Climate*, **35**, 669–686, https://doi.org/10.1175/JCLI-D-21-0282.1.

Lindsay, R., M. Wensnahan, A. Schweiger, and J. Zhang, 2014: Evaluation of seven different atmospheric reanalysis products in the Arctic. *J. Climate*, **27**, 2588–2606, https://doi.org/10.1175/JCLI-D-13-00014.1.

Liu, Y., and J. R. Key, 2014: Less winter cloud aids summer 2013 Arctic sea ice return from 2012 minimum. *Environ. Res. Lett.*, **9**, 044002, https://doi.org/10.1088/1748-9326/9/4/044002.

Liu, Z., and Coauthors, 2022: Atmospheric forcing dominates winter Barents-Kara Sea ice variability on interannual to decadal time scales. *Proc. Natl. Acad. Sci. USA*, **119**, e2120770119, https://doi.org/10.1073/pnas.2120770119.

Luo, B., D. Luo, L. Wu, L. Zhong, and I. Simmonds, 2017: Atmospheric circulation patterns which promote winter Arctic sea ice decline. *Environ. Res. Lett.*, **12**, 054017, https://doi.org/10.1088/1748-9326/aa69d0.

——, and Coauthors, 2023: Origins of Barents-Kara sea-ice interannual variability modulated by the Atlantic pathway of El Niño–Southern Oscillation. *Nat. Commun.*, **14**, 585, https://doi.org/10.1038/s41467-023-36136-5.

Luo, D., Y. Xiao, Y. Yao, A. Dai, I. Simmonds, and C. L. E. Franzke, 2016: Impact of Ural blocking on winter warm Arctic–cold Eurasian anomalies. Part I: Blocking-induced amplification. *J. Climate*, **29**, 3925–3947, https://doi.org/10.1175/JCLI-D-15-0611.1.

Madonna, E., G. Hes, C. Li, C. Michel, and P. Y. F. Siew, 2020: Control of Barents Sea wintertime cyclone variability by large-scale atmospheric flow. *Geophys. Res. Lett.*, **47**, e2020GL090322, https://doi.org/10.1029/2020GL090322.

Matsumura, S., X. Zhang, and K. Yamazaki, 2014: Summer Arctic atmospheric circulation response to spring Eurasian snow cover and its possible linkage to accelerated sea ice decrease. *J. Climate*, **27**, 6551–6558, https://doi.org/10.1175/JCLI-D-13-00549.1.

Maykut, G. A., 1978: Energy exchange over young sea ice in the central Arctic. *J. Geophys. Res.*, **83**, 3646–3658, https://doi.org/10.1029/JC083iC07p03646.

Meier, W. N., J. S. Stewart, A. Windnagel, and F. M. Fetterer, 2021: NOAA/NSIDC climate data record of passive microwave sea ice concentration, version 4. NSIDC, accessed 28 August 2023, https://doi.org/10.7265/efmz-2t65.

——, ——, ——, and ——, 2022: Comparison of hemispheric and regional sea ice extent and area trends from NOAA and NASA passive microwave-derived climate records. *Remote Sens.*, **14**, 619, https://doi.org/10.3390/rs14030619.

Merkouriadi, I., G. E. Liston, R. M. Graham, and M. A. Granskog, 2020: Quantifying the potential for snow-ice formation in the Arctic Ocean. *Geophys. Res. Lett.*, **47**, e2019GL085020, https://doi.org/10.1029/2019GL085020.

Mills, C. M., and J. E. Walsh, 2014: Synoptic activity associated with sea ice variability in the Arctic. *J. Geophys. Res. Atmos.*, **119**, 12 117–12 131, https://doi.org/10.1002/2014JD021604.

Mortin, J., G. Svensson, R. G. Graversen, M.-L. Kapsch, J. C. Stroeve, and L. N. Boisvert, 2016: Melt onset over Arctic sea ice controlled by atmospheric moisture transport. *Geophys. Res. Lett.*, **43**, 6636–6642, https://doi.org/10.1002/2016GL069330.

Notz, D., F. A. Haumann, H. Haak, J. H. Jungclaus, and J. Marotzke, 2013: Arctic sea-ice evolution as modeled by Max Planck Institute for Meteorology's Earth system model. *J. Adv. Model. Earth Syst.*, **5**, 173–194, https://doi.org/10.1002/jame.20016.

——, and Coauthors, 2020: Arctic sea ice in CMIP6. *Geophys. Res. Lett.*, **47**, e2019GL086749, https://doi.org/10.1029/2019GL086749.

Nygård, T., R. G. Graversen, P. Uotila, T. Naakka, and T. Vihma, 2019: Strong dependence of wintertime Arctic moisture and cloud distributions on atmospheric large-scale circulation. *J. Climate*, **32**, 8771–8790, https://doi.org/10.1175/JCLI-D-19-0242.1.

——, M. Tjernström, and T. Naakka, 2021: Winter thermodynamic vertical structure in the Arctic atmosphere linked to large-scale circulation. *Wea. Climate Dyn.*, **2**, 1263–1282, https://doi.org/10.5194/wcd-2-1263-2021.

Outten, S., and Coauthors, 2023: Reconciling conflicting evidence for the cause of the observed early 21st century Eurasian cooling. *Wea. Climate Dyn.*, **4**, 95–114, https://doi.org/10.5194/wcd-4-95-2023.

Park, H.-S., and A. L. Stewart, 2016: An analytical model for wind-driven Arctic summer sea ice drift. *Cryosphere*, **10**, 227–244, https://doi.org/10.5194/tc-10-227-2016.

——, S. Lee, S.-W. Son, S. B. Feldstein, and Y. Kosaka, 2015: The impact of poleward moisture and sensible heat flux on Arctic winter sea ice variability. *J. Climate*, **28**, 5030–5040, https://doi.org/10.1175/JCLI-D-15-0074.1.

——, A. L. Stewart, and J.-H. Son, 2018: Dynamic and thermodynamic impacts of the winter Arctic Oscillation on summer sea ice extent. *J. Climate*, **31**, 1483–1497, https://doi.org/10.1175/JCLI-D-17-0067.1.

Petty, A. A., M. M. Holland, D. A. Bailey, and N. T. Kurtz, 2018: Warm Arctic, increased winter sea ice growth? *Geophys. Res. Lett.*, **45**, 12 922–12 930, https://doi.org/10.1029/2018GL079223.

Pithan, F., and Coauthors, 2018: Role of air-mass transformations in exchange between the Arctic and mid-latitudes. *Nat. Geosci.*, **11**, 805–812, https://doi.org/10.1038/s41561-018-0234-1.

Polyakov, I. V., M. Mayer, S. Tietsche, and A. Y. Karpechko, 2022: Climate change fosters competing effects of dynamics and thermodynamics in seasonal predictability of Arctic sea ice. *J. Climate*, **35**, 2849–2865, https://doi.org/10.1175/JCLI-D-21-0463.1.

Post, E., and Coauthors, 2013: Ecological consequences of sea-ice decline. *Science*, **341**, 519–524, https://doi.org/10.1126/science.1235225.

Rheinlænder, J. W., R. Davy, E. Ólason, P. Rampal, C. Spensberger, T. D. Williams, A. Korosov, and T. Spengler, 2022: Driving mechanisms of an extreme winter sea ice breakup event in the Beaufort Sea. *Geophys. Res. Lett.*, **49**, e2022GL099024, https://doi.org/10.1029/2022GL099024.

Rigor, I. G., J. M. Wallace, and R. L. Colony, 2002: Response of sea ice to the Arctic Oscillation. *J. Climate*, **15**, 2648–2663, https://doi.org/10.1175/1520-0442(2002)015<2648:ROSITT>2.0.CO;2.

Rinke, A., M. Maturilli, R. M. Graham, H. Matthes, D. Handorf, L. Cohen, S. R. Hudson, and J. C. Moore, 2017: Extreme cyclone events in the Arctic: Wintertime variability and trends. *Environ. Res. Lett.*, **12**, 094006, https://doi.org/10.1088/1748-9326/aa7def.

Schreiber, E. A. P., and M. C. Serreze, 2020: Impacts of synoptic-scale cyclones on Arctic sea-ice concentration: A systematic analysis. *Ann. Glaciol.*, **61**, 139–153, https://doi.org/10.1017/aog.2020.23.

Screen, J. A., and I. Simmonds, 2010: The central role of diminishing sea ice in recent Arctic temperature amplification. *Nature*, **464**, 1334–1337, https://doi.org/10.1038/nature09051.

Serreze, M. C., and J. Stroeve, 2015: Arctic sea ice trends, variability and implications for seasonal ice forecasting. *Philos. Trans. Roy. Soc.*, **A373**, 20140159, https://doi.org/10.1098/rsta.2014.0159.

Siew, P. Y. F., C. Li, S. P. Sobolowski, and M. P. King, 2020: Intermittency of Arctic–mid-latitude teleconnections: Stratospheric pathway between autumn sea ice and the winter North Atlantic Oscillation. *Wea. Climate Dyn.*, **1**, 261–275, https://doi.org/10.5194/wcd-1-261-2020.

Singh, H. A., P. J. Rasch, and B. E. J. Rose, 2017: Increased ocean heat convergence into the high latitudes with CO_2 doubling enhances polar-amplified warming. *Geophys. Res. Lett.*, **44**, 10 583–10 591, https://doi.org/10.1002/2017GL074561.

Skific, N., J. A. Francis, and J. J. Cassano, 2009: Attribution of projected changes in atmospheric moisture transport in the Arctic: A self-organizing map perspective. *J. Climate*, **22**, 4135–4153, https://doi.org/10.1175/2009JCLI2645.1.

Smith, K. L., L. M. Polvani, and L. B. Tremblay, 2018: The impact of stratospheric circulation extremes on minimum Arctic Sea ice extent. *J. Climate*, **31**, 7169–7183, https://doi.org/10.1175/JCLI-D-17-0495.1.

Sorteberg, A., and B. Kvingedal, 2006: Atmospheric forcing on the Barents Sea winter ice extent. *J. Climate*, **19**, 4772–4784, https://doi.org/10.1175/JCLI3885.1.

——, and J. E. Walsh, 2008: Seasonal cyclone variability at 70°N and its impact on moisture transport into the Arctic. *Tellus*, **60A**, 570–586, https://doi.org/10.1111/j.1600-0870.2007.00314.x.

Stroeve, J. C., D. Schroder, M. Tsamados, and D. Feltham, 2018: Warm winter, thin ice? *Cryosphere*, **12**, 1791–1809, https://doi.org/10.5194/tc-12-1791-2018.

Tyrlis, E., E. Manzini, J. Bader, J. Ukita, H. Nakamura, and D. Matei, 2019: Ural blocking driving extreme Arctic sea ice loss, cold Eurasia, and stratospheric vortex weakening in autumn and early winter 2016–2017. *J. Geophys. Res. Atmos.*, **124**, 11 313–11 329, https://doi.org/10.1029/2019JD031085.

Wang, Z., J. Walsh, S. Szymborski, and M. Peng, 2020: Rapid Arctic sea ice loss on the synoptic time scale and related atmospheric circulation anomalies. *J. Climate*, **33**, 1597–1617, https://doi.org/10.1175/JCLI-D-19-0528.1.

Webster, M., and Coauthors, 2018: Snow in the changing sea-ice systems. *Nat. Climate Change*, **8**, 946–953, https://doi.org/10.1038/s41558-018-0286-7.

——, C. Parker, L. Boisvert, and R. Kwok, 2019: The role of cyclone activity in snow accumulation on Arctic sea ice. *Nat. Commun.*, **10**, 5285, https://doi.org/10.1038/s41467-019-13299-8.

Wegmann, M., Y. Orsolini, A. Weisheimer, B. van den Hurk, and G. Lohmann, 2021: Impact of Eurasian autumn snow on the winter North Atlantic Oscillation in seasonal forecasts of the 20th century. *Wea. Climate Dyn.*, **2**, 1245–1261, https://doi.org/10.5194/wcd-2-1245-2021.

Wernli, H., and L. Papritz, 2018: Role of polar anticyclones and mid-latitude cyclones for Arctic summertime sea-ice melting. *Nat. Geosci.*, **11**, 108–113, https://doi.org/10.1038/s41561-017-0041-0.

Wittek, P., S. C. Gao, I. S. Lim, and L. Zhao, 2013: Somoclu: An efficient parallel library for self-organizing maps. *J. Stat. Software*, **78** (9), 1–21, https://doi.org/10.18637/jss.v078.i09.

Woods, C., and R. Caballero, 2016: The role of moist intrusions in winter Arctic warming and sea ice decline. *J. Climate*, **29**, 4473–4485, https://doi.org/10.1175/JCLI-D-15-0773.1.

——, ——, and G. Svensson, 2013: Large-scale circulation associated with moisture intrusions into the Arctic during winter. *Geophys. Res. Lett.*, **40**, 4717–4721, https://doi.org/10.1002/grl.50912.

Wu, Y., and K. L. Smith, 2016: Response of Northern Hemisphere midlatitude circulation to Arctic amplification in a simple atmospheric general circulation model. *J. Climate*, **29**, 2041–2058, https://doi.org/10.1175/JCLI-D-15-0602.1.

Yang, W., and G. Magnusdottir, 2017: Springtime extreme moisture transport into the Arctic and its impact on sea ice concentration. *J. Geophys. Res. Atmos.*, **122**, 5316–5329, https://doi.org/10.1002/2016JD026324.

Yu, L., S. Zhong, M. Zhou, D. H. Lenschow, and B. Sun, 2019: Revisiting the linkages between the variability of atmospheric circulations and Arctic melt-season sea ice cover at multiple time scales. *J. Climate*, **32**, 1461–1482, https://doi.org/10.1175/JCLI-D-18-0301.1.

——, ——, T. Vihma, and B. Sun, 2021: Attribution of late summer early autumn Arctic sea ice decline in recent decades. *npj Climate Atmos. Sci.*, **4**, 3, https://doi.org/10.1038/s41612-020-00157-4.

Zhang, J., and D. A. Rothrock, 2003: Modeling global sea ice with a thickness and enthalpy distribution model in generalized curvilinear coordinates. *Mon. Wea. Rev.*, **131**, 845–861, https://doi.org/10.1175/1520-0493(2003)131<0845:MGSIWA>2.0.CO;2.

Zhang, P., Y. Wu, I. R. Simpson, K. L. Smith, X. Zhang, B. De, and P. Callaghan, 2018: A stratospheric pathway linking a colder Siberia to Barents-Kara Sea sea ice loss. *Sci. Adv.*, **4**, eaat6025, https://doi.org/10.1126/sciadv.aat6025.

Zheng, C., M. Ting, Y. Wu, N. Kurtz, C. Orbe, P. Alexander, R. Seager, and M. Tedesco, 2022: Turbulent heat flux, downward longwave radiation, and large-scale atmospheric circulation associated with wintertime Barents–Kara Sea extreme sea ice loss events. *J. Climate*, **35**, 3747–3765, https://doi.org/10.1175/JCLI-D-21-0387.1.